



# Enhanced methane monitoring: A globally harmonized daily 0.1° XCH<sub>4</sub> through machine learning-based fusion of GOSAT, GOSAT-2, and TROPOMI

Jebun Naher Keya<sup>1,\*</sup>, Yejin Kim<sup>1,\*</sup>, Hyunyoung Choi<sup>1</sup>, Junggho Im<sup>1,2,3,4,\*</sup>

5 <sup>1</sup>Department of Civil, Urban, Earth, & Environmental Engineering, Ulsan National Institute of Science and Technology, Ulsan, 44919, Republic of Korea

<sup>2</sup>Graduate School of Carbon Neutrality, Ulsan National Institute of Science and Technology, Ulsan, 44919, Republic of Korea

<sup>3</sup>Artificial Intelligence Graduate School, Ulsan National Institute of Science and Technology, Ulsan, 44919, Republic of Korea

10 <sup>4</sup>Department of Environmental Resources Engineering, State University of New York College of Environmental Science and Forestry, Syracuse, NY 13210, USA

\*Corresponding Author: Junggho Im ([ersgis@unist.ac.kr](mailto:ersgis@unist.ac.kr))

\*These authors contributed equally to this work.

**Abstract.** Accurate global monitoring of atmospheric methane (CH<sub>4</sub>) is essential for tracking progress toward climate  
15 mitigation targets such as the Global Methane Pledge (GMP). Ground-based measurement networks are too sparse to provide sufficient spatial coverage, while satellite-derived retrievals are hindered by systematic biases and uncertainties, limiting their reliability for consistent global monitoring. We present the first global fusion of GOSAT, GOSAT-2, and TROPOMI to generate a globally consistent daily 0.1° land dataset for 2020–2023 for enhanced global XCH<sub>4</sub> mapping. The framework employs a three-step machine-learning (ML) approach: (1) sensor-specific bias correction using TCCON observations, (2)  
20 cross-sensor harmonization to GOSAT-2, the sensor with the strongest post-correction TCCON agreement, and (3) priority-based fusion. Tree-based ensemble regressors were trained with satellite retrieval parameters to reduce systematic biases and inter-sensor discrepancies. Independent validation at three withheld TCCON stations demonstrates robust generalization of the fused product ( $R^2 = 0.81$ , RMSE = 10.78 ppb), outperforming standard and operational bias-corrected satellite products and previously reported ML-based approaches. Regional assessments show that fusion substantially improves data availability  
25 and reduces systematic errors, delivering up to 12% relative coverage gains and 33–94% bias reductions compared to TROPOMI operational products in challenging regions (South Asia, Amazon Basin, Eastern Siberia). The fused dataset reveals intensifying positive XCH<sub>4</sub> anomalies (+60 ppb) over South Asia, East Asia, and Central Africa during 2020–2023, linked to MODIS-derived agricultural and urban land classes as well as known oil and gas fields. The dataset provides a scalable resource for regional CH<sub>4</sub> emissions assessment and continuous monitoring, with the framework extendable to upcoming  
30 satellite missions (GOSAT-GW, CO2M) for long-term GMP progress tracking.

## 1 Introduction

Methane (CH<sub>4</sub>) is a potent greenhouse gas (GHG), contributing approximately 0.6 °C of global warming since the pre-industrial era and accounting for nearly 30% of the observed increase in global mean surface temperature (Naik et al., 2021;  
35 IEA, 2025). Despite lower atmospheric concentrations than CO<sub>2</sub>, its global warming potential is 28 times higher over a 100-year horizon (Myhre et al., 2014). Its high radiative efficiency, combined with a relatively short atmospheric lifetime due to oxidation by hydroxyl radicals (OH), makes CH<sub>4</sub> an especially effective target for near-term climate mitigation (Prather et al., 2012; Nisbet et al., 2020). Recent observations show that CH<sub>4</sub> levels have been rising at an unprecedented rate, with 2020–2022 marking the fastest growth since systematic monitoring began (Suniois et al., 2025). Major CH<sub>4</sub> sources include



40 anthropogenic activities (livestock farming, rice cultivation, fossil-fuel exploitation, and waste management) and natural  
wetland emissions (Saunois et al., 2025). Reflecting the urgency of mitigation, the Global Methane Pledge (GMP) launched  
at the 26th Conference of the Parties (COP26) aims to reduce global CH<sub>4</sub> emissions by at least 30% from 2020 levels by 2030  
(IEA, 2022). Accurate XCH<sub>4</sub> quantification is therefore essential for identifying emission sources and evaluating progress  
toward climate goals.

45 Ground-based monitoring systems such as the Total Carbon Column Observing Network (TCCON) provide high-precision  
XCH<sub>4</sub> measurements and serve as key reference data for satellite validation and bias correction. Despite their accuracy,  
TCCON sites are limited in number and spatially sparse (Lorente et al., 2021), leaving large observational gaps across Africa,  
South America, and large parts of Asia. Satellite platforms help address these limitations by providing broad spatial coverage.  
The GHGs Observing Satellite (GOSAT), GOSAT-2, and the TROPOspheric Monitoring Instrument (TROPOMI) have  
50 enabled global-scale XCH<sub>4</sub> mapping and have been widely used for emission estimation and inverse modeling (Qu et al., 2021;  
Worden et al., 2022; Nesser et al., 2024; Maasakkers et al., 2019; Janardanan et al., 2020). However, these instruments exhibit  
distinct trade-offs in spatial resolution, revisit frequency, and retrieval accuracy. GOSAT and GOSAT-2 provide high spectral  
resolution (0.2 cm<sup>-1</sup>) but limited spatial and temporal coverage with ~10 km circular footprints and multi-day revisit intervals  
(Kuze et al., 2016; Suto et al., 2021). In contrast, TROPOMI offers near-daily global coverage at finer spatial resolution (5.5  
55 × 7 km<sup>2</sup>) but suffers from larger retrieval uncertainties due to lower spectral sensitivity and greater vulnerability to clouds and  
aerosols (Jacob et al., 2022; Hasekamp et al., 2021; Umezawa et al., 2025). As a result, no single satellite can offer both the  
accuracy and coverage desirable for robust global-scale XCH<sub>4</sub> monitoring, making multi-sensor data fusion necessary.  
However, merging multiple sources first requires addressing the systematic biases inherent to each sensor to ensure inter-  
sensor consistency.

60 Previous bias correction studies have typically relied on statistical regression trained against TCCON observations, accounting  
for surface albedo, aerosol loading, and viewing geometry (Inoue et al., 2016; Lorente et al., 2021). However, such methods  
can struggle to capture nonlinear, sensor-specific bias structures. Machine learning (ML) approaches, including Random Forest  
(RF), Light Gradient Boosting Machine (LightGBM), and eXtreme Gradient Boosting (XGBoost), have demonstrated  
improved bias correction performance by learning complex relationships between retrieval errors and environmental or  
65 observational predictors (Balasus et al., 2023; Schneising et al., 2022; Li et al., 2024).  
Despite these advances, several limitations remain. Some studies improve spatial coverage but retain substantial residual bias  
(Li et al., 2024), whereas others reduce systematic bias by applying global offsets to match TCCON means (Balasus et al.,  
2023; Parker et al., 2020), an approach that can ignore regional variations in sensor bias. Moreover, most prior work has  
focused on single-sensor enhancement or limited dual-sensor combinations (e.g., GOSAT + TROPOMI), leaving the potential  
70 of multi-sensor fusion underexplored (Fan et al., 2024; Balasus et al., 2023; Li et al., 2024). In contrast, XCO<sub>2</sub> research has  
increasingly adopted multi-platform fusion (e.g., OCO-2, OCO-3, GOSAT, and GOSAT-2) as a standard approach (Chen et  
al., 2024; Wang et al., 2022), while comprehensive global XCH<sub>4</sub> fusion products remain comparatively scarce. To the best of  
our knowledge, GOSAT-2 has not yet been incorporated into a global XCH<sub>4</sub> fusion product, despite its improved spectral  
performance and expanded coverage relative to GOSAT.

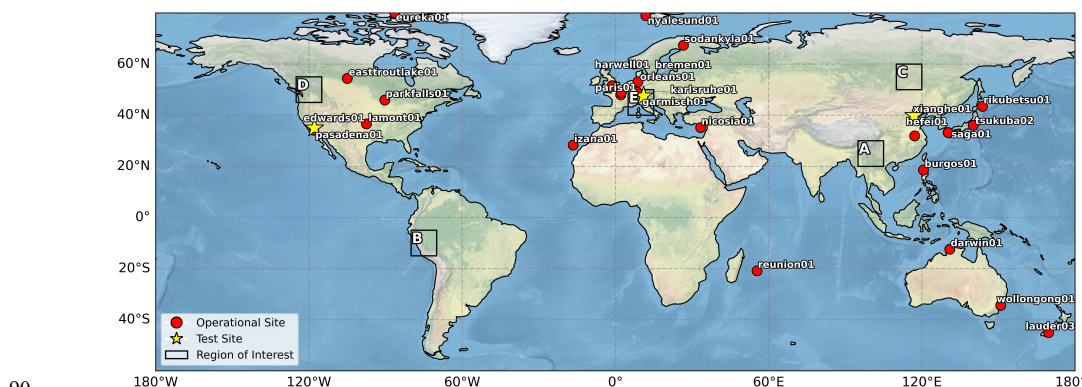
75 To address these gaps and enable consistent global XCH<sub>4</sub> monitoring, we develop an ML-based multi-sensor harmonization  
and fusion framework that (1) corrects sensor-specific biases using TCCON observations, (2) harmonizes all satellite retrievals  
to the most accurate sensor (GOSAT-2), and (3) fuses the harmonized retrievals to maximize daily spatial coverage while  
preserving accuracy. The resulting product provides global daily XCH<sub>4</sub> over land (60°S–80°N) at 0.1° resolution for 2020–  
2023, with improved accuracy and spatiotemporal coverage, compared to individual sensor retrievals. This enhanced dataset  
80 enables more reliable regional emission analysis, hotspot identification, and source characterization.



## 2 Datasets

### 2.1 Ground XCH<sub>4</sub> observations

TCCON is a global network of ground-based Fourier transform spectrometers (FTSs) that record direct solar spectra in the near-infrared (NIR) region (Wunch et al., 2011). TCCON serves as a benchmark dataset for validating satellite-derived XCH<sub>4</sub> because its measurements are minimally affected by aerosol loading, air mass uncertainty, and surface-reflectance variability compared with SWIR satellite retrievals (Dils et al., 2014; Malina et al., 2022). We obtained latest TCCON GGG2020 dataset from the TCCON data archive (<https://tccodata.org/>, last accessed 26 December 2025) spanning January 2020 to December 2023, covering the overlapping observation period of TROPOMI, GOSAT, and GOSAT-2. Stations used in this study are shown in Fig. 1 and listed in Table S1.



90 **Figure 1.** Study domain and TCCON stations (GGG2020 XCH<sub>4</sub>) used during 2020–2023. Red circles denote stations used for model training/validation. Yellow stars indicate independent test stations held out from training and used only for evaluation of the fused XCH<sub>4</sub> product. Black boxes (A–E) denote regions of interest used for regional analyses in Section 4.3.

### 2.2. Satellite XCH<sub>4</sub> products

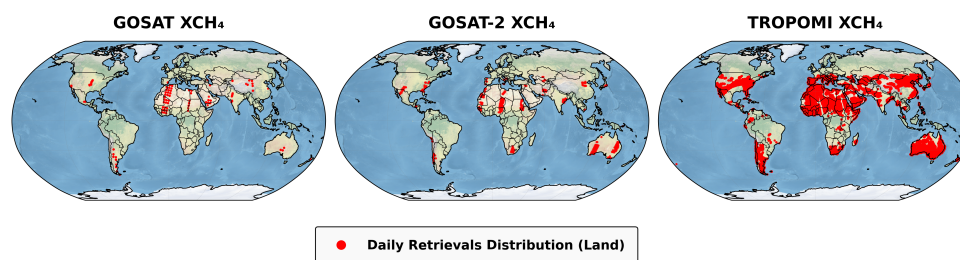
95 This study used XCH<sub>4</sub> products from TROPOMI, GOSAT, and GOSAT-2. All three missions retrieve XCH<sub>4</sub> using full-physics algorithms that simultaneously estimate surface albedo, atmospheric scattering, and trace-gas concentrations from SWIR and NIR spectra (Butz et al., 2011). However, full-physics retrievals are sensitive to clouds, aerosols, and surface heterogeneity, increasing retrieval bias and reducing data availability in high-aerosol regions and complex terrain (Jacob et al., 2022; Umezawa et al., 2025). GOSAT features ~30 times higher spectral resolution than TROPOMI, enhancing retrieval precision, while TROPOMI provides near-daily global coverage but is more susceptible to light-path errors (Hu et al., 2018; Qu et al., 2021). These contrasting characteristics reflect an inherent trade-off between sampling density and retrieval accuracy. Table 1 summarizes mission specifications, and Fig. 2 illustrates daily sampling patterns.

**Table 1.** Key specifications of GOSAT, GOSAT-2, and Sentinel-5P/TROPOMI XCH<sub>4</sub> products used in this study.

	GOSAT	GOSAT-2	TROPOMI
Local overpass time	13:00	13:00	13:30
Pixel size	10.5 km diameter	9.7 km diameter	5.5×7 km <sup>2</sup>
Pixel separation	260–280 km	260–280 km	None
Coverage	global	global	global
Revisit time	3 days	6 days	Sub-daily
Retrieval type	full physics	full physics	full physics
Retrieval version	v03.05	v02.00	version 02.04.00
Number of retrievals per day (pixel) <sup>a</sup>	360	908	386,233



105 <sup>a</sup>The number of XCH<sub>4</sub> retrievals per day represents the average soundings calculated per day over the full study period from 1  
January 2020 to 31 December 2023.



110 **Figure 2. Spatial distribution of daily XCH<sub>4</sub> retrievals over land on 1 January 2020 from GOSAT, GOSAT-2, and TROPOMI. Red markers indicate native pixel locations of individual soundings and are enlarged for visualization purposes.**

### 2.2.1. GOSAT

GOSAT (also known as *Ibuki*), launched in 2009, carries the Thermal and NIR Sensor for carbon Observation Fourier transform spectrometer (TANSO-FTS) and the TANSO Cloud and Aerosol Imager (CAI) in a sun-synchronous orbit at 666 km (Kuze et al., 2009). TANSO-FTS measures high-resolution spectra in the SWIR and thermal infrared bands, which are  
115 used to retrieve column abundances of CO<sub>2</sub> and CH<sub>4</sub> (Yoshida et al., 2011). We used the NIES SWIR L2 CH<sub>4</sub> product (v03.05) from GOSAT Data Archive Service (GDAS: <https://data2.gosat.nies.go.jp/>, last accessed 26 December 2025), which provides both bias-uncorrected (hereafter standard) and bias-corrected retrievals calibrated against TCCON GGG2014 (Inoue et al., 2016). The standard product was used as ML model input, while the bias-corrected product was used for comparison.

### 2.2.2 GOSAT-2

120 GOSAT-2, the successor of GOSAT was launched in 2018, carries upgraded TANSO-FTS-2 and CAI-2 with an intelligent cloud-avoidance pointing strategy, enabling enhanced sensitivity and expanded spatial coverage (Suto et al., 2021; Imasu et al., 2023). GOSAT-2 extends Band 3 spectral coverage to 2.33 μm (compared to 2.08 μm for GOSAT), capturing additional CH<sub>4</sub> absorption features. We used the SWIR Level-2 full-physics XCH<sub>4</sub> product (v02.00; hereafter standard) from the GOSAT-2 archive (<https://data2.gosat.nies.go.jp/>, last accessed 26 December 2025). To ensure high data reliability, only  
125 retrievals with quality flag = 0 were retained for bias-correction modeling.

### 2.2.3 TROPOMI

TROPOMI, the sole payload on ESA's Sentinel-5 Precursor (S5P) mission launched in 2017, is a nadir-viewing push-broom hyperspectral imaging spectrometer that measures radiance from the ultraviolet (UV) to the SWIR (Veeckind et al., 2012). CH<sub>4</sub> retrievals are derived using the RemoTeC algorithm (Hasekamp et al., 2021), and the sun-synchronous orbit with an  
130 approximately 2,600 km swath width enables near-daily global mapping of atmospheric CH<sub>4</sub>. We used the S5P Level-2 XCH<sub>4</sub> product (S5P\_L2\_CH4\_HiR) from NASA Goddard Earth Sciences Data and Information Services Center (GES DISC; <https://doi.org/10.5270/S5P-3lcdqiv>, last accessed 26 December 2025). This dataset provides both uncorrected XCH<sub>4</sub> (hereafter standard) and the posteriori albedo-dependent bias corrected XCH<sub>4</sub> (Lorente et al., 2021), along with associated retrieval parameters. For consistency with GOSAT and GOSAT-2, we selected standard XCH<sub>4</sub> retrievals with a quality  
135 assurance flag qa\_value > 0.5 as model input, while the official bias-corrected product was used for comparison.



### 3 Methodology

To address limitations of single-sensor CH<sub>4</sub> retrievals and inter-satellite inconsistencies, we developed an integrated ML framework that combines bias correction, cross-sensor harmonization, and multi-sensor fusion of XCH<sub>4</sub> retrievals from TROPOMI, GOSAT, and GOSAT-2. The framework produces a globally harmonized daily 0.1° land XCH<sub>4</sub> product for 2020–

140 2023 through three hierarchical steps (Fig. 3):

**Step 1:** Sensor-specific bias correction using TCCON as the calibration standard.

**Step 2:** Inter-satellite harmonization by aligning all datasets to the most accurate sensor (bias-corrected GOSAT-2).

**Step 3:** Multi-sensor fusion to maximize daily spatial coverage while preserving accuracy.

We define the systematic retrieval bias for a given satellite observation as:

145 
$$\Delta_{\text{Bias}} = XCH_{4,\text{Satellite}} - XCH_{4,\text{Reference}} \quad (1)$$

where  $XCH_{4,\text{Satellite}}$  denotes the standard (uncorrected) satellite retrieval and  $XCH_{4,\text{Reference}}$  denotes the reference value (TCCON in Step 1; bias-corrected GOSAT-2 in Step 2). For BC, we used ensemble tree-based regressors (RF and XGBoost) due to their strong performance and stability in tabular regression with nonlinear interactions (Hwang et al., 2023; Shwartz-Ziv and Armon, 2022). For GOSAT and GOSAT-2, the predictor set additionally included co-retrieved XCO<sub>2</sub>-related variables because CH<sub>4</sub> and CO<sub>2</sub> are retrieved simultaneously from the same SWIR spectra using a shared full-physics forward model (Butz et al., 2010). Scattering-induced light-path errors often affect both gases in a correlated manner (Oshio et al., 2020). As TROPOMI does not retrieve CO<sub>2</sub>, only XCH<sub>4</sub> retrieval parameters were selected based on established practice (Balasus et al., 2023). Using these parameters, mission-specific BC models were trained to predict bias ( $\hat{\Delta}_{\text{Bias}}$ ) and the predicted bias was subtracted from the original retrieval:

155 
$$XCH_{4,BC} = XCH_{4,\text{Satellite}} - \hat{\Delta}_{\text{Bias}} \quad (2)$$

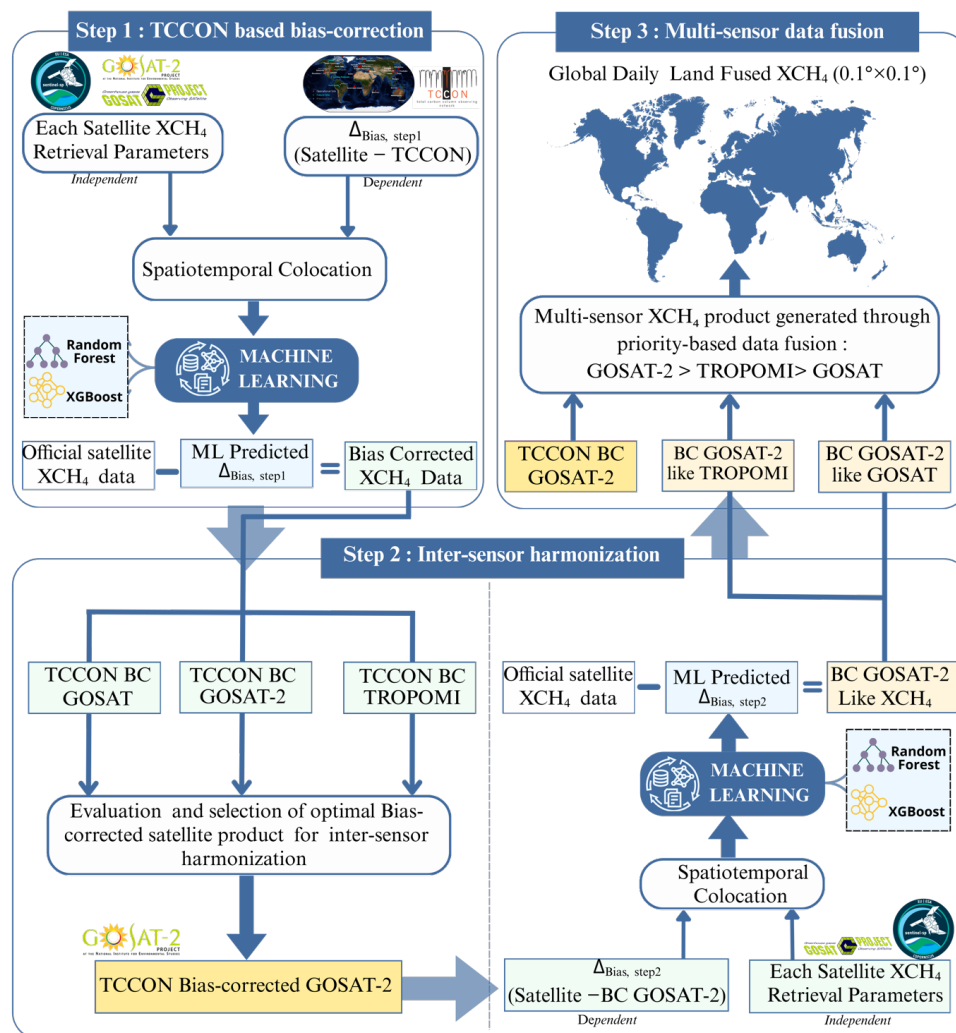


**Figure 3. Overview of the machine learning (ML)-based bias correction (BC) and data fusion framework used to generate the Fused XCH<sub>4</sub> product.**

160 **3.1. Data preprocessing and colocation**

Reliable colocation between satellite retrievals and reference observations is essential for bias correction and validation. The sparse global distribution of TCCON sites prevents perfectly coincident measurements (Zhou et al., 2016). We therefore constructed collocated training pairs using satellite-specific spatiotemporal and elevation constraints following official validation strategies (Sha et al., 2021; Yoshida et al., 2023). Using the criteria in Table 2, we first established Step 1 between each satellite and TCCON. To ensure adequate temporal representation across 2020–2023 and sufficient training samples, TCCON sites with fewer than 20 collocated observations (i.e., bremen01, eureka01, nicosia01, and rikubetsu01) were excluded. We then constructed Step 2 inter-satellite collocations, pairing GOSAT and TROPOMI observations with TCCON calibrated GOSAT-2 using the thresholds in Table 2.

170 **Table 2. Colocation criteria used for TCCON-based bias correction (Step 1) and inter-satellite harmonization (Step 2). All thresholds were chosen based on satellite-specific characteristics and standard validation practices.**



Step	Reference	Satellite	Radius	Time window	Altitude difference
Step1	TCCON	GOSAT, GOSAT-2	200 km	±30 min	< 250 m
		TROPOMI	100 km	±1 hour	
Step2	Bias-corrected	GOSAT	20 km	Same date	< 200 m
	GOSAT-2	TROPOMI	5 km	±1 hour	-

### 3.2. ML-based bias correction and harmonization

While GOSAT and TROPOMI provide official bias-corrected products (Inoue et al., 2016; Lorente et al., 2021), GOSAT-2  
 175 does not. To treat all sensors consistently, we developed a unified ML framework using TCCON as the calibration standard.  
 Previous studies improved TROPOMI XCH<sub>4</sub> by aligning to GOSAT official (Fan et al., 2024) or GOSAT proxy data (Balasus  
 et al., 2023; Li et al., 2024), which applies a single global offset to force mean bias to zero and is available only through 2021  
 (Parker et al., 2020). Our approach directly calibrates each sensor against TCCON, enabling spatially and temporally adaptive  
 bias correction throughout 2020–2023 and data-driven harmonization reference selection.

#### 180 3.2.1 Step 1: TCCON-based bias correction

For each satellite, we trained ML models using satellite–TCCON collocated pairs to predict the systematic bias between raw  
 satellite retrievals and TCCON:

$$\Delta_{\text{Bias, step1}} = XCH_{4,\text{Satellite}} - XCH_{4,\text{TCCON}} \quad (3)$$

Satellite-specific retrieval parameters were used as predictors to model systematic error in the raw XCH<sub>4</sub> retrievals. Because  
 185 each mission provides a large number of candidate retrieval parameters (>100), we applied a three-stage feature selection  
 procedure:

1. Correlation screening: Pearson and Spearman analyses to rank predictors based on linear and monotonic  
 associations with  $\Delta_{\text{Bias, step1}}$ .
2. Recursive feature elimination (RFE): RFE with cross-validation to identify a compact predictor subset.
- 190 3. Refinement: final adjustment using feature-importance rankings from preliminary models.

The final predictor lists are provided in Tables S2–S4. The trained model predicts  $\hat{\Delta}_{\text{Bias, step1}}$  and the bias-corrected product is  
 computed using Eq. (2).

#### 3.2.2 Step 2: Inter-sensor harmonization

To select a harmonization reference, we evaluated the Step 1 bias-corrected outputs from all three sensors against common  
 195 TCCON observations. GOSAT-2 exhibited the highest agreement with TCCON and was therefore selected as the  
 harmonization reference (detailed results in Section 4.2). Using inter-satellite collocations (Table 2), we developed ML models  
 to reduce sensor-to-sensor discrepancies relative to calibrated GOSAT-2:

$$\Delta_{\text{Bias, step2}} = XCH_{4,\text{Satellite}} - XCH_{4,\text{BC GOSAT-2}} \quad (4)$$

where  $XCH_{4,\text{Satellite}}$  is the standard retrieval from the target sensor (GOSAT or TROPOMI) and  $XCH_{4,\text{BC GOSAT-2}}$  is the  
 200 Step-1 bias-corrected GOSAT-2 retrieval. Feature selection followed the same three-stage procedure as in Section 3.2.1  
 (correlation screening, RFE, and importance refinement). Final predictor lists are provided in Tables S4–S5. We trained ML  
 models to predict  $\hat{\Delta}_{\text{Bias, step2}}$  and generated GOSAT-2-like harmonized products by subtracting the predicted bias:

$$XCH_{4,\text{Harmonized}} = XCH_{4,\text{Satellite}} - \hat{\Delta}_{\text{Bias, step2}} \quad (5)$$



### 205 3.3. Step 3: Data Fusion

The fusion step integrates harmonized satellite datasets into a single daily 0.1° gridded product. We adopted a hierarchical priority-based fusion strategy (Chen et al., 2024), ranking datasets by their validation performance against TCCON and inter-sensor consistency. Because GOSAT-2 was selected as the harmonization reference and exhibits the strongest independent agreement with TCCON, it was assigned the highest priority. Based on the Step-2 evaluation, the final ranking used for fusion

210 was:

GOSAT-2 (BC) → TROPOMI (GOSAT-2-like) → GOSAT (GOSAT-2-like)

For each day and each 0.1° grid cell  $(x, y)$ , the fused product was defined as:

$$XCH_{4,Fused}(x, y) = \begin{cases} XCH_{4,GOSAT-2}(x, y), & \text{if available} \\ XCH_{4,TROPOMI}(x, y), & \text{else if available} \\ XCH_{4,GOSAT}(x, y), & \text{else if available} \\ NaN, & \text{otherwise} \end{cases} \quad (6)$$

This rule retains the highest-priority valid observation at each location and time, thereby improving both spatial coverage and  
215 precision of the fused daily XCH<sub>4</sub> product.

### 3.4 Model evaluation

The spatial and temporal generalization performance of the BC was quantitatively evaluated using step-specific validation strategies. In Step 1, spatial generalization was assessed using leave-one-site-out cross-validation (LOSOCV) to account for site-to-site differences in background XCH<sub>4</sub> levels and spatial heterogeneity. Temporal generalization was evaluated using  
220 leave-one-month-out cross-validation (LOMOCV) and leave-one-year-out cross-validation (LOYOCV) to account for interannual variability and growth trends. In Step 2, leave-one-band-out cross-validation (LOBOCV) was applied across 11 latitudinal zones (60°S–80°N; Fig. S1) to account for latitudinal gradients in CH<sub>4</sub> emissions (Maasackers et al. 2019), with temporal validation using LOMOCV and LOYOCV. Model performance was evaluated using three standard metrics: coefficient of determination (R<sup>2</sup>), root mean square error (RMSE) and mean absolute error (MAE) and (Equations S1–S3).

## 225 4 Results and discussion

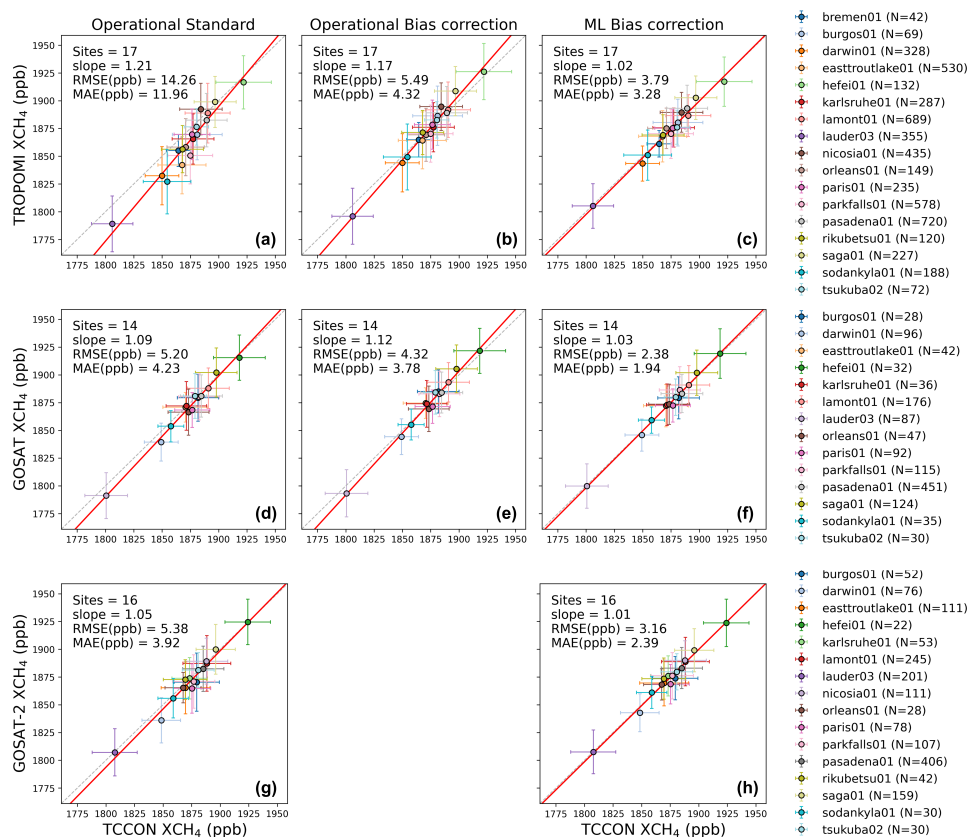
### 4.1. Overall validation against TCCON

We evaluated the spatiotemporal generalization performance of official satellite products and ML-based bias-correction against TCCON. In the LOSOCV results (Fig. 4), the standard products systematically deviated from the 1:1 line, with pronounced negative biases at low-XCH<sub>4</sub> sites such as Darwin01, Lauder03, and Sodankylä01 (Figs. 4a, d, g; see Fig. 1 for  
230 site locations). These sites are located in the Southern Hemisphere or high latitudes, where challenging retrieval conditions (e.g., high solar zenith angle and high surface albedo) and limited TCCON sampling can amplify errors. In addition, operational bias corrections tuned around typical global XCH<sub>4</sub> levels (≈1850–1900 ppb) can leave larger residual deviations at the low and high tails.

In contrast, the ML-based correction tightened agreement for all sensors, reducing both RMSE and MAE. Sensor-specific  
235 models were selected (Table S6; : XGBoost for TROPOMI, RF for GOSAT and GOSAT-2). For TROPOMI, the RMSE decreased from 14.26 ppb (standard) and 5.49 ppb (operational bias-corrected) to 3.28 ppb (ML), corresponding to 73% and 40%, reductions (Fig. 4a–c). For GOSAT, RMSE reductions of 54% and 45% were achieved relative to the operational standard and bias-corrected products, respectively, while GOSAT-2 showed a 41% reduction relative to the operational standard (Fig. 4d–h). Site-wise error statistics (Figs. S2–S4) confirmed these improvements, with ML-based correction  
240 reducing both station-wise mean bias ( $\mu$ ) and variability ( $\sigma$ ), indicating more uniform performance under spatially



heterogeneous conditions. Given a global XCH<sub>4</sub> growth rate of ~8–14 ppb yr<sup>-1</sup> during the study period (NOAA GML; [https://gml.noaa.gov/ccgg/trends\\_ch4/](https://gml.noaa.gov/ccgg/trends_ch4/); last accessed 26 December 2025), these reductions are large enough to influence long-term trend interpretation.

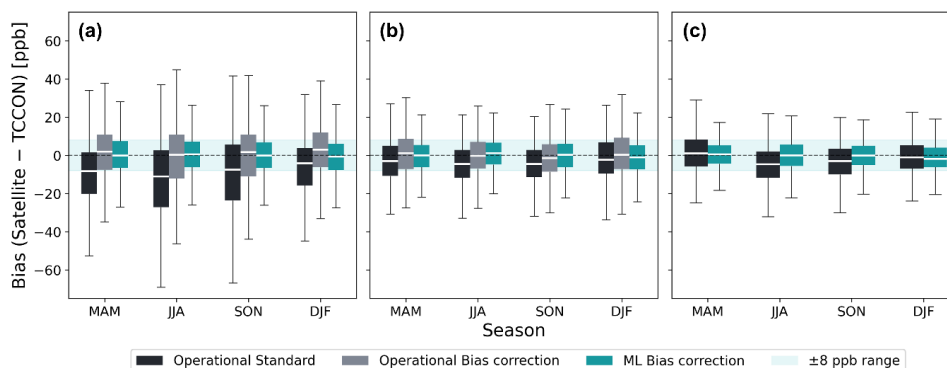


245 **Figure 4.** Site-wise scatterplots of column-averaged dry-air methane (XCH<sub>4</sub>) between Total Carbon Column Observing Network (TCCON) and satellite products; (a–c) TROPOMI XCH<sub>4</sub>, (d–f) GOSAT XCH<sub>4</sub>, (g–h) GOSAT-2 XCH<sub>4</sub> for the operational standard and operational bias-corrected products, and machine learning (ML) based bias-corrected result (under leave-one-site-out cross-validation), respectively. Each marker represents the mean XCH<sub>4</sub> at one TCCON site over the study period, with horizontal and vertical error bars indicating one standard deviation of TCCON and satellite XCH<sub>4</sub>, respectively. Red lines denote least-squares linear regression fits.

250

The LOMOCV results further highlighted differences in temporal generalization (Fig. 5). Across sensors, the standard products showed negative medians and broad interquartile ranges (IQRs) and larger biases in summer and autumn. Operational bias correction shifted the median bias toward zero but retained stronger seasonal variability than the ML-based correction. The ML-based correction maintained seasonal medians near zero and constrained the IQR to within ±8 ppb, indicating more stable performance under seasonal variability.

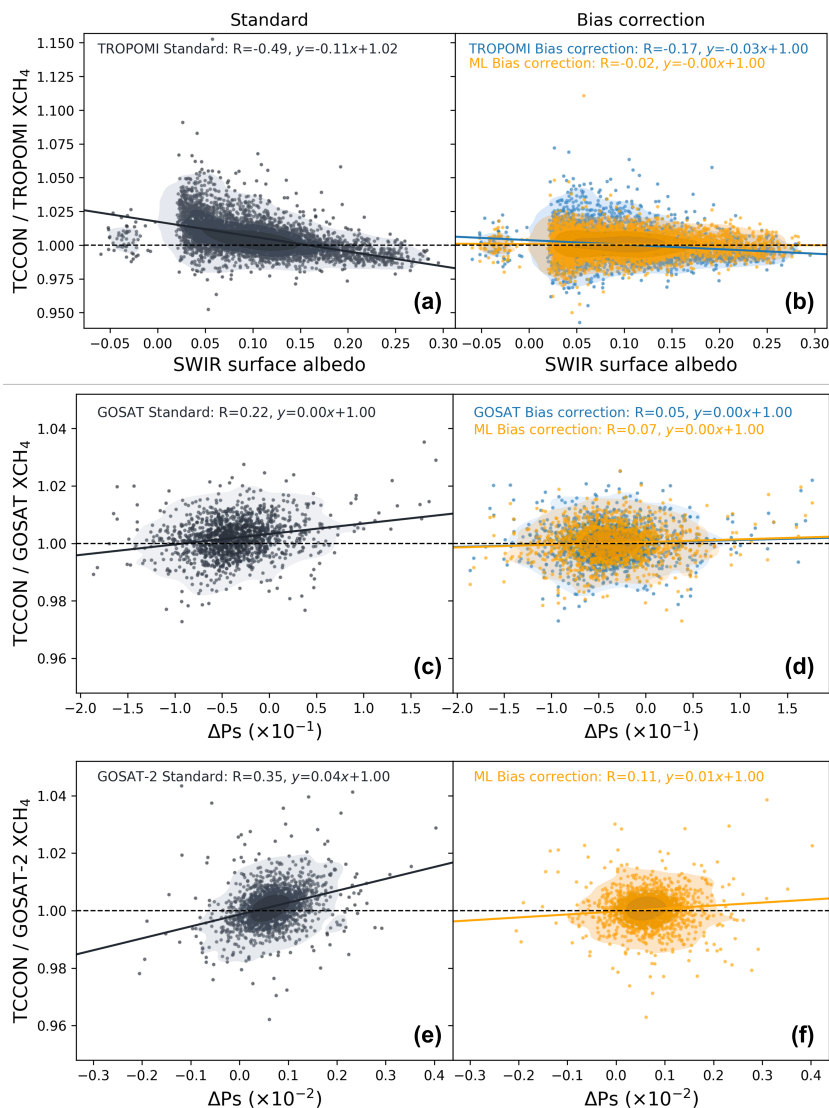
255



260 **Figure 5. Seasonal distributions of XCH<sub>4</sub> bias (Satellite – TCCON) under leave-one-month-out cross-validation results. Box-and-whisker plots summarize seasonal bias distributions for (a) TROPOMI, (b) GOSAT, and (c) GOSAT-2 across correction strategies (operational bias correction, and ML-based bias correction). Boxes indicate the interquartile range (IQR) with the median shown as a horizontal white line. The shaded band marks the ±8 ppb range around zero bias.**

Figure 6 further illustrates condition-dependent biases by relating the XCH<sub>4</sub> ratio (TCCON/ satellite) to key retrieval variables. For TROPOMI, the standard product shows a strong negative dependence on SWIR surface albedo ( $R = -0.49$ ; Fig. 6a), consistent with known sensitivity to scattering-related light-path errors under low-albedo conditions (Lorente et al., 2021; Balasus et al., 2023; Li et al., 2024). Bias correction substantially reduces this dependence (Fig. 6b), yielding near-zero correlation ( $R = -0.02$ ) and indicating that albedo-driven bias is largely mitigated. For the GOSAT series, operational bias correction is implemented as a multiple linear regression using explanatory variables (e.g.,  $\Delta P$ s, XH<sub>2</sub>O, airmass, and  $\Delta T$ ) (Inoue et al., 2016; Yoshida et al., 2023). Consistently,  $\Delta P$ s dependence is weak for GOSAT ( $R = 0.22$ ; Fig. 6c) and more evident for GOSAT-2 ( $R = 0.35$ ; Fig. 6e) in the standard products, and it is reduced after correction (Figs. 6d, f). Overall, the ML-based correction reduces not only mean bias but also bias sensitivity to key retrieval conditions across sensors.

265  
270



275 **Figure 6.** Dependence of (TCCON/Satellite) XCH<sub>4</sub> ratios on key retrieval variables and its reduction after bias correction. (a,b) (TCCON/TROPOMI) XCH<sub>4</sub> ratio as a function of SWIR surface albedo for the standard product (a) and after bias correction (b). (c–f) Same as (a,b) but for GOSAT and GOSAT-2 as a function of surface pressure difference ( $\Delta P_s$ ): standard product in (c,e) and bias-corrected results in (d,f). Solid lines denote the fitted least-squares regressions, and the dashed horizontal line indicates the unbiased reference level (ratio = 1). The Pearson correlation coefficient (R) and regression equation are reported in each panel.

280

#### 4.2. Inter-satellite harmonization

Multi-sensor fusion requires minimizing inter-sensor inconsistencies by defining a common reference scale. Table 3 compares the ML-based bias-corrected products using common samples to select an appropriate reference sensor. GOSAT-2 achieved the highest accuracy ( $R^2 = 0.67$ ; RMSE = 10.67 ppb) and was therefore selected as harmonization reference.

285



**Table 3. Accuracy comparison of machine learning (ML) based bias-corrected XCH<sub>4</sub> from three satellites sensors (TROPOMI, GOSAT, GOSAT-2), evaluated against Total Carbon Column Observing Network using collocated common samples (N=309). Boldface indicates the satellite with the best performance for each error metric.**

Metrics	TROPOMI	GOSAT	GOSAT-2
R <sup>2</sup>	0.60	0.60	<b>0.67</b>
MAE (ppb)	9.49	9.21	<b>8.38</b>
RMSE (ppb)	11.78	11.92	<b>10.67</b>

290

To improve cross-sensor consistency, the GOSAT and TROPOMI products were calibrated to the bias-corrected GOSAT-2 scale (i.e., generating “GOSAT-2-like” XCH<sub>4</sub>). Across the evaluated algorithms, XGBoost yielded the best harmonization performance (Table S7). Figure 7 shows distributional shifts before and after calibration: after harmonization, bias distributions for GOSAT and TROPOMI moved toward near-zero mean bias relative to GOSAT-2 and their spread is reduced. TROPOMI exhibited slightly higher agreement with GOSAT-2 than GOSAT and provided approximately six times more collocated observations (Table S7). Accordingly, the fusion priority was set to GOSAT-2 → TROPOMI → GOSAT to balance reference consistency and sampling density and to enhance robustness of the fused XCH<sub>4</sub> product.

295

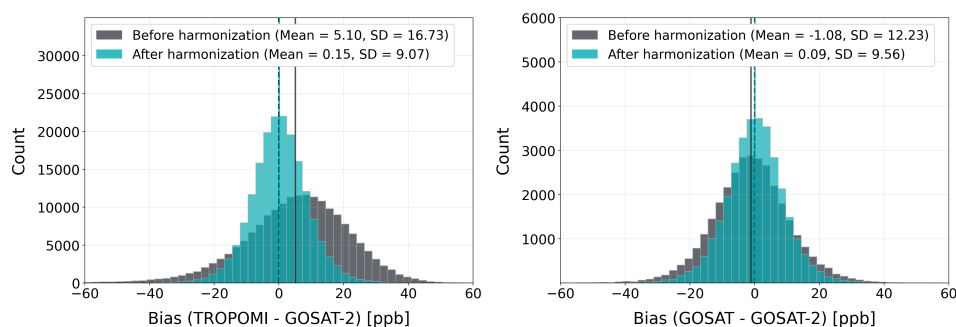


**Figure 7. Inter-satellite harmonization to the ML bias-corrected GOSAT-2 scale. Distributions of XCH<sub>4</sub> bias relative to the ML-based bias-corrected GOSAT-2 product (a): TROPOMI – GOSAT-2; (b): GOSAT – GOSAT-2) before and after cross-satellite harmonization. Solid vertical lines denote the mean bias for each distribution, and the legend reports the corresponding mean and standard deviation (SD).**

Figure 8 evaluates the fused XCH<sub>4</sub> product at three independent TCCON sites (Xianghe01, Edwards01, and Garmisch01) and includes a comparison with the Blended TROPOMI+GOSAT product of Balasus et al. (2023). These sites were excluded from the TCCON-based bias correction in Step 1 to assess generalization under independent conditions. The three stations represent distinct environments : rural site (Xianghe, China; mean = 1903.16 ppb), urban (Edwards, USA; mean = 1880.37 ppb), and mountainous (Garmisch, Germany; mean = 1872.98 ppb). Across all sites, the fused XCH<sub>4</sub> showed strong agreement with TCCON (R<sup>2</sup> = 0.81, RMSE = 10.78 ppb; Fig. 8a). The time series further indicates that the fused product reproduces temporal variability, while reducing inter-sensor offsets relative to the individual satellite products (Fig. 8b). For 2022, the fused product achieved higher accuracy than the Blended XCH<sub>4</sub> product at the same locations, (R<sup>2</sup> = 0.74, RMSE = 10.38 ppb vs. R<sup>2</sup> = 0.67, RMSE = 11.82 ppb; Fig. 8c), which may reflect the use of a harmonized multi-sensor framework that incorporates the higher-accuracy GOSAT-2 product.

315

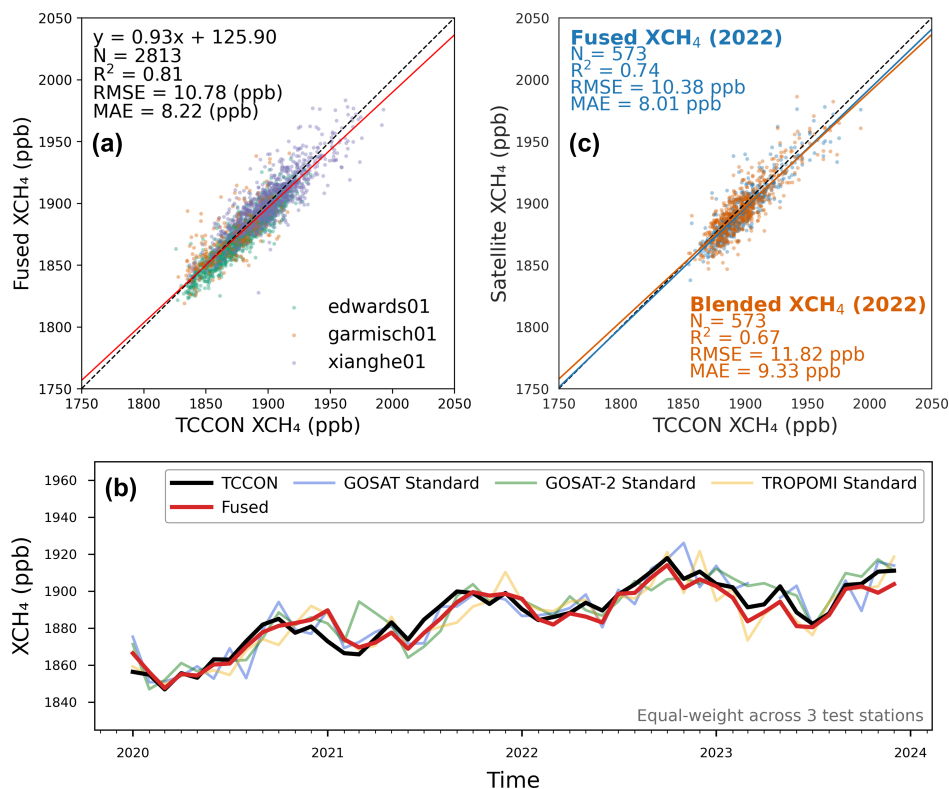


Figure 8. Independent validation of the Fused XCH<sub>4</sub> at three TCCON test stations and comparison with a Blended product (Balasus et al., 2023). (a) Scatter plot of Fused XCH<sub>4</sub> versus TCCON XCH<sub>4</sub> at three independent sites (Xianghe01, Edwards01, and Garmisch01); colors indicate individual stations. The red line denotes the fitted regression. (b) Time series of station-mean XCH<sub>4</sub> averaged across the three test stations (equal-weight mean), comparing TCCON, Fused, and the standard products from GOSAT, GOSAT-2, and TROPOMI. (c) Comparison against TCCON for 2022 at the same test stations, contrasting the Fused XCH<sub>4</sub> (blue) with the Blended XCH<sub>4</sub> product based on TROPOMI and GOSAT (orange). The solid-colored lines denote fitted regressions, respectively.

### 325 4.3. Coverage improvements from multi-satellite fusion

The fused XCH<sub>4</sub> product achieved annual global land coverage of 87.1%, 86.9%, 86.8%, and 88.1% for 2020–2023, corresponding to improvements of 0.45–0.74 percentage points over TROPOMI alone (Fig. S5a). Although global annual averages show modest gains, multi-sensor fusion yields substantial regional enhancements where individual sensors face systematic retrieval limitations.

330 To quantify fusion benefits under challenging retrieval conditions for TROPOMI, we examined five case-study regions (ROIs; Fig. 1) in 2023 representing diverse environments and emission regimes: South Asia (ROI-A) and the Amazon Basin (ROI-B) as cloudy tropical regions with aerosol impacts; Eastern Siberia (ROI-C) as high-latitude wetlands with seasonal snow/ice constraints; the Pacific Northwest (ROI-D) as complex coastal terrain; and Central Europe (ROI-E) as Alpine topography. Compared with TROPOMI, coverage improvements ranged from ~2.5% to ~9.5%, with the largest gain in South Asia (Fig. 9a).

335

We assessed product quality for the fused and TROPOMI operational products (standard and operational bias-corrected) using TCCON-calibrated (bias-corrected) GOSAT-2 as a reference. Fusion substantially reduced bias, achieving errors within ±5 ppb across all ROIs and reducing bias by 33–94% relative to TROPOMI products (Fig. 9b). Source attribution maps



illustrate how the GOSAT series spatially complements TROPOMI coverage in 2023 (Fig. 9c): GOSAT-2 provides the majority of additional observations, particularly filling monsoon-related gaps in South Asia and cloudy tropical regions, while GOSAT supplements coverage over Alpine terrain, where complex topography challenges both TROPOMI and GOSAT-2 retrievals.

Fusion also improves temporal resilience during periods of single-mission data loss. Missing VIIRS cloud-screening information in July–August 2022 and August 2023 (Borsdorff et al., 2024) led to substantial gaps in TROPOMI XCH<sub>4</sub>, which were partially filled by overlapping GOSAT and GOSAT-2 observations (Fig. S5b). This multi-sensor complementarity highlights the importance of global-scale fusion for comprehensive CH<sub>4</sub> monitoring.

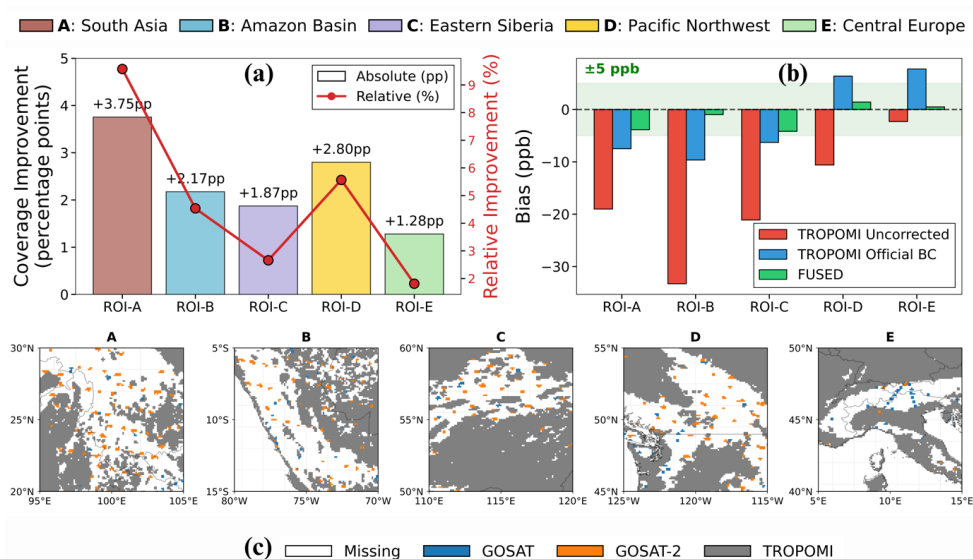


**Figure 9. Regional performance assessment of multi-sensor XCH<sub>4</sub> fusion in 2023 across five regions representing distinct retrieval challenges. (a) Coverage enhancement showing absolute gain in percentage points (bars, left axis) and relative improvement (line, right axis). (b) Bias reduction relative to TCCON-calibrated GOSAT-2; green shading indicates  $\pm 5$  ppb target zone. (c) Bottom panels show annually dominant sensor per pixel based on valid retrieval frequency in 2023 (GOSAT: blue, GOSAT-2: orange, TROPOMI: grey, missing data: white). Orange and blue pixels indicate locations where GOSAT-2 or GOSAT had more valid retrievals than TROPOMI.**

355

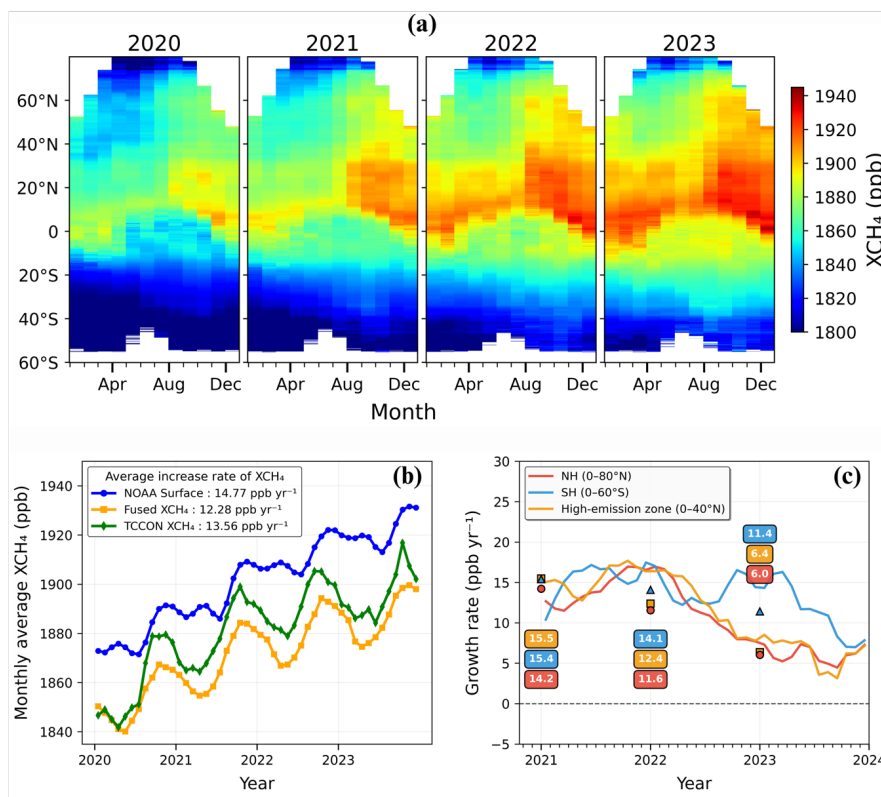
#### 4.4. Global XCH<sub>4</sub> mapping and spatiotemporal analysis

The fused dataset reveals distinct spatiotemporal patterns across 2020–2023. Time–latitude diagrams (Fig. 10a) show a persistent interhemispheric gradient of 30–40 ppb between the Northern Hemisphere (NH) and Southern Hemisphere (SH). Elevated XCH<sub>4</sub> is consistently observed in the northern subtropical belt (0–40°N), where mean concentrations increased from 1872.72 ppb to 1906.98 ppb over the study period (+34.26 ppb), exceeding the global mean increase. While the highest concentrations remained in the north, the fused product captured a progressive southward expansion in XCH<sub>4</sub> increases beginning in 2021, consistent with recent findings (Umezawa et al., 2025).

To quantify global growth rates, we compared the monthly global average of the fused dataset with independent observations from TCCON ground-based columns and NOAA marine surface records ([https://gml.noaa.gov/ccgg/trends\\_ch4/](https://gml.noaa.gov/ccgg/trends_ch4/), last accessed: 26 December 2026). The fused product captures a sustained rise from approximately 1850 ppb in early 2020 to nearly 1900 ppb by late 2023, corresponding to a mean global growth rate of 12.28 ppb yr<sup>-1</sup> (Fig. 10b). This agrees well with TCCON (13.56 ppb yr<sup>-1</sup>) and NOAA (14.77 ppb yr<sup>-1</sup>), supporting the ability of the fused dataset to represent large-scale atmospheric



CH<sub>4</sub> trends. Interannual growth rates exhibited strong regional variability (Fig. 10c). The NH (0–80°N), SH (60°S–0°), and the high-emission zone (0–40°N) all peaked in 2021 at 14.2, 15.4, and 15.5 ppb yr<sup>-1</sup>, respectively, consistent with record global  
 370 XCH<sub>4</sub> increases reported for that period (Saunio et al., 2025). After 2021, growth rates decelerated through 2022–2023, reaching approximately 6.0 ppb yr<sup>-1</sup> (NH), 11.4 ppb yr<sup>-1</sup> (SH), and 6.4 ppb yr<sup>-1</sup> (high-emission zone) by 2023, consistent with recent inverse modeling estimates (Pendergrass et al., 2025).



375 **Figure 10.** Spatiotemporal patterns of fused XCH<sub>4</sub> (2020–2023). (a) Monthly latitudinal distribution of XCH<sub>4</sub> concentrations at 0.1° resolution for 2020–2023. (b) Global mean XCH<sub>4</sub> time series comparison between the fused product (orange), NOAA marine surface measurements (blue), and TCCON ground-based observations (green). (c) Monthly (solid line) and yearly (marker) growth rates from year-over-year for the Northern Hemisphere (NH: 0–80°N, red), Southern Hemisphere (SH: 0–60°S, blue), and high-emission zone (0–40°N, orange).

380 To highlight emission hotspots relative to the global baseline, we computed annual anomalies by subtracting the four-year mean (1869.95 ppb) from each year’s XCH<sub>4</sub> field (Fig. 11). By 2023, positive anomalies exceeding +60 ppb were apparent over South Asia, East Asia, and Central Africa, with maxima over the Indo-Gangetic Plain and the Ganges–Brahmaputra delta (Fig. 11d). The shift in global mean anomaly from –16.74 ppb (2020) to +14.16 ppb (2023) indicates increasing XCH<sub>4</sub> accumulation over the study period.

385

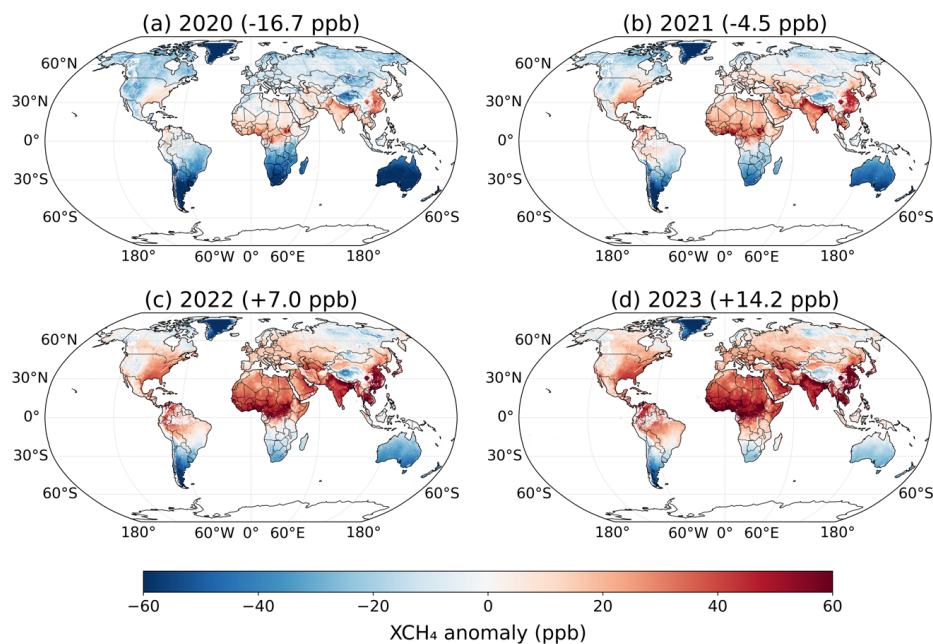
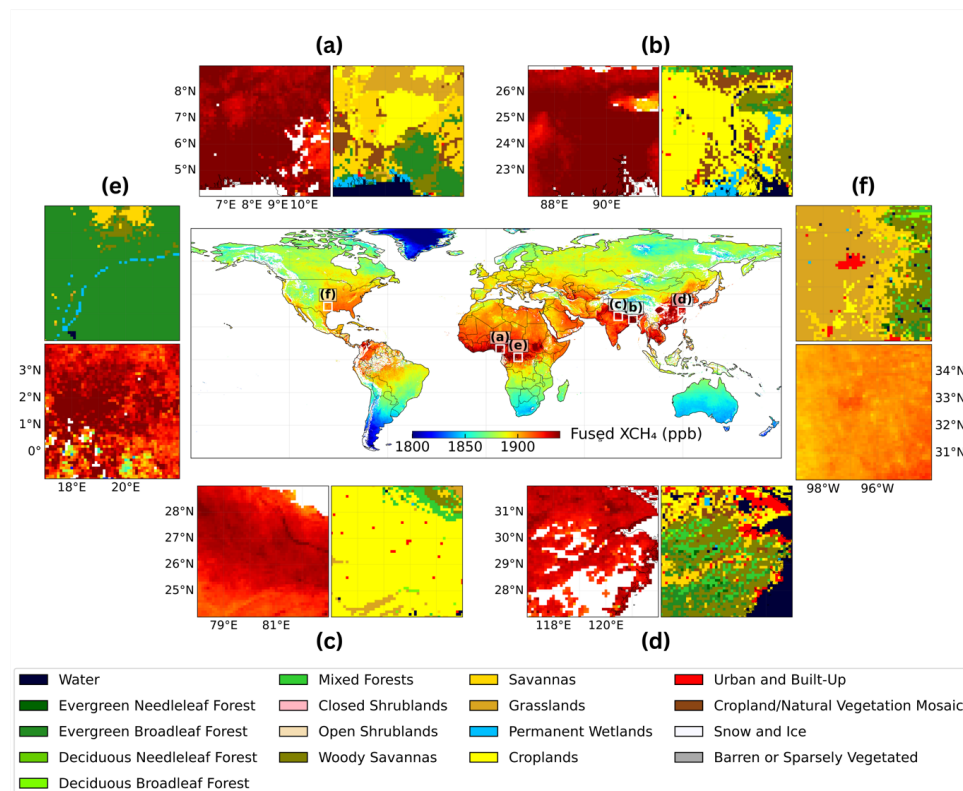


**Figure 11. Annual XCH<sub>4</sub> anomaly maps for (a) 2020, (b) 2021, (c) 2022, and (d) 2023 relative to the four-year mean. Parentheses show global mean anomalies (ppb). Positive (red) and negative (blue) shading indicate regions with XCH<sub>4</sub> above and below the four-year baseline, respectively.**

390 To interpret drivers of elevated concentrations, we examined high-anomaly regions in 2023 using MODIS MCD12Q1 land-  
cover information (Fig. 12). Hotspots showed distinct land-cover signatures: the Niger Delta (a) exhibited strong anomalies  
over a mix of croplands, evergreen broadleaf forests, coastal wetlands, and urban areas associated with petroleum infrastructure  
(Sj et al., 2024); the Ganges–Brahmaputra Delta (b) showed the largest anomaly over rice paddies and permanent wetlands;  
the Indo-Gangetic Plain (c) and Yangtze River Delta (d) displayed persistent enhancements over irrigated croplands and  
expanding metropolitan areas; the Congo Basin (e) showed elevated concentrations over tropical peatlands and evergreen  
395 forests; and the southern United States (f) showed enhancements over the Permian Basin, consistent with documented oil-and-  
gas emissions (Zhang et al., 2020). The spatial correspondence between enhanced XCH<sub>4</sub> and wetland/cropland/urban land  
classes demonstrates the fused product’s ability to resolve regional emission patterns.

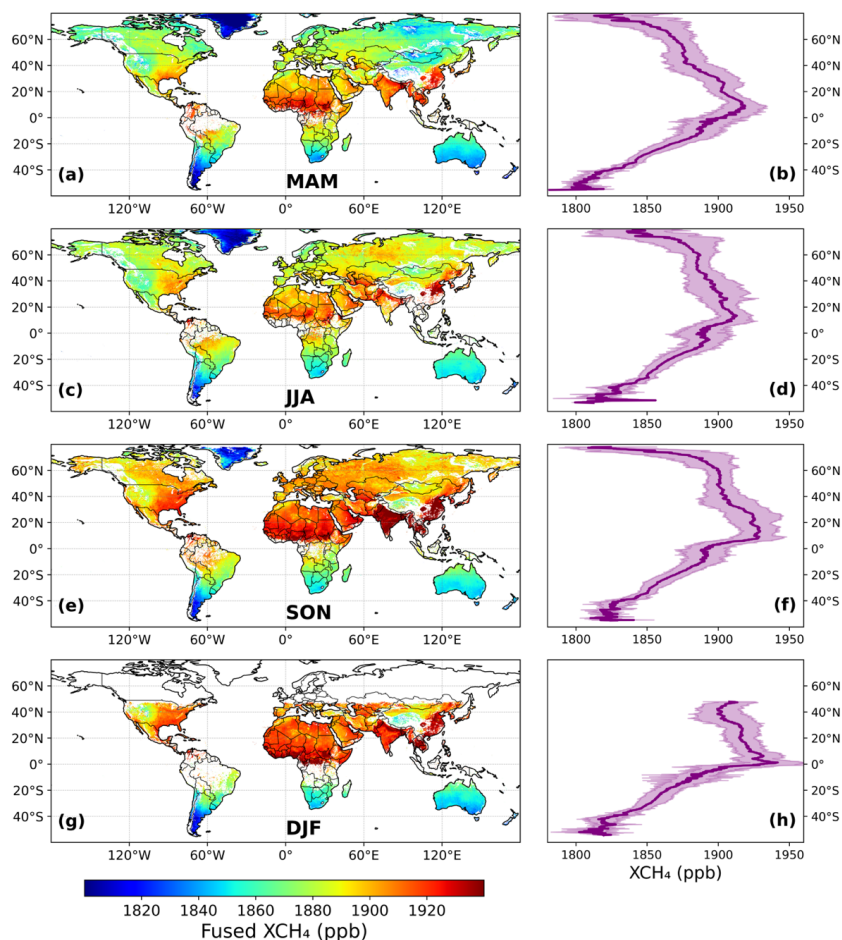


400 **Figure 12. Regional XCH<sub>4</sub> emission hotspots and corresponding land-cover characteristics for 2023. The central map displays the global distribution of fused XCH<sub>4</sub> concentrations with six representative high-emission regions marked (a–f). Each regional panel pair shows XCH<sub>4</sub> concentrations (left) and MODIS MCD12Q1 land-cover classifications (right) for the Niger Delta (a), Ganges–Brahmaputra Delta (b), Indo-Gangetic Plain (c), Yangtze River Delta (d), Congo Basin (e), and southern United States (f). Land-cover legend follows the MODIS MCD12Q1 LC\_Type1 classification.**

405

Finally, we examined seasonal patterns of global XCH<sub>4</sub> in 2023. To preserve localized XCH<sub>4</sub> enhancements, zonal-mean profiles were calculated at native 0.1° latitude resolution (Fig. 13), and seasonal statistics were summarized for major latitude zones (Table S8). The NH (0–80°N) exhibited the largest seasonal amplitude (32.14 ppb), peaking in winter (DJF; 1915.36 ppb) and reaching a minimum in spring (MAM; 1883.22 ppb). Within the NH, the high-emission zone (0–40°N) remained elevated year-round (≈1901 ppb in JJA to ≈1918 ppb in SON/DJF) with a moderate amplitude (16.50 ppb). In contrast, the SH (60°S–0°) showed a smaller amplitude (6.77 ppb), varying between 1850.66 ppb (MAM) and 1857.43 ppb (JJA). The pronounced NH seasonality reflects strong source variability from wetland and agricultural emissions, whereas the smoother SH cycle is more strongly governed by the OH sink than by local emissions (East et al., 2024).

410



415

**Figure 13. Seasonal distributions of fused XCH<sub>4</sub> concentrations and latitudinal gradients in 2023. Left panels (a, c, e, g) show seasonal mean XCH<sub>4</sub> concentrations at 0.1° resolution for March–April–May (MAM), June–July–August (JJA), September–October–November (SON), and December–January–February (DJF). Right panels (b, d, f, h) display corresponding zonal mean profiles (solid purple line) with shaded regions representing spatial variability ( $\pm 1\sigma$  standard deviation) across each latitude band. Latitudes with data coverage below 2% were excluded from zonal mean calculations to ensure statistical robustness. Regional definitions and seasonal statistics are detailed in Table S8.**

420

#### 4.5. Limitations

While the framework substantially improves retrieval accuracy across sensors, several limitations should be noted. First, the fused dataset uses a fixed sensor-priority strategy (GOSAT-2 → TROPOMI → GOSAT) based on overall accuracy and sampling density, which may introduce regional bias because local observing conditions can favor a non-prioritized sensor. Second, the current dataset does not provide pixel-level uncertainty estimates. Although the fused product achieves an RMSE of approximately 10.8 ppb at independent test sites, this global summary statistic does not describe how errors vary across regions or observing conditions. Third, although the fusion framework improves robustness, global annual coverage gains are modest (0.45–0.74 percentage points over TROPOMI). Fourth, ML-based correction in this study relies primarily on retrieval parameters to model systematic biases; incorporating external environmental covariates (e.g., temperature, humidity, and wind) may further reduce regional biases and improve generalization (Qu et al., 2025). Finally, the 0.1° resolution supports regional-scale analyses but remains insufficient for resolving fine-scale emission sources detectable by emerging high-resolution

430



missions (e.g., EMIT or GHGSat). Future work could address these limitations via adaptive sensor weighting, uncertainty  
435 quantification, and integration of additional environmental covariates.

## 5 Conclusion

This study presents the first global multi-sensor fusion framework that integrates XCH<sub>4</sub> retrievals from GOSAT,  
GOSAT-2, and TROPOMI. Using a three-step ML strategy (1) TCCON-calibrated bias correction (2) inter-sensor  
440 harmonization, and (3) fusion, we produced a globally harmonized daily 0.1° land XCH<sub>4</sub> dataset for 2020–2023. Independent  
evaluation at withheld TCCON sites demonstrates strong generalization ( $R^2 = 0.81$ , RMSE = 10.78 ppb), outperforming the  
standard and operationally bias-corrected satellite products.

A key outcome is that GOSAT-2 provides an effective anchor for cross-sensor harmonization, offering high agreement  
with TCCON while maintaining broader sampling than GOSAT. Regional assessments show that fusion improves data  
445 availability in retrieval-limited environments, increasing coverage by ~2.5% to ~9.5% depending on region, and reducing bias  
by 33–94% compared to the TROPOMI operational products.

The fused product reproduces key spatiotemporal characteristics of atmospheric XCH<sub>4</sub>, including interannual hemispheric  
variability and persistent emission hotspots in tropical and subtropical regions associated with wetlands, agriculture, and fossil-  
fuel infrastructure. These capabilities support emission source attribution and evaluation of mitigation strategies at regional  
450 scales. The proposed framework is extensible to upcoming missions (GOSAT-GW, CO2M), enabling enhanced monitoring.  
Continued advances in multi-sensor harmonization and uncertainty characterization will be crucial for supporting progress  
toward the GMP target of a 30% CH<sub>4</sub> emission reduction by 2030.

## Code and data availability

The fusion pipeline and example code for accessing and working with the fused XCH<sub>4</sub> dataset are available at  
455 [https://github.com/jnkeya/Fused\\_XCH4](https://github.com/jnkeya/Fused_XCH4). The fused XCH<sub>4</sub> dataset, including daily and monthly mean products for 2020–2023,  
is publicly available on Zenodo at <https://doi.org/10.5281/zenodo.18714293>. All input datasets are publicly available as  
described in Sect. 2.

## Author contributions

460 J.K.: Writing – original draft, Visualization, Validation, Methodology, Investigation, Formal analysis, Conceptualization. Y.K.:  
Writing – original draft, Visualization, Validation, Methodology, Investigation, Formal analysis, Conceptualization. H.C.:  
Writing – review & editing. J.I.: Writing – review & editing, Supervision, Methodology, Funding acquisition,  
Conceptualization.

## Competing interest

465 The authors declare that they have no conflict of interest.



## Acknowledgments

## References

- Balagus, N., Jacob, D. J., Lorente, A., Maasackers, J. D., Parker, R. J., Boesch, H., ... & Varon, D. J. (2023). A blended TROPOMI+ GOSAT satellite data product for atmospheric methane using machine learning to correct retrieval biases. *Atmospheric Measurement Techniques*, 16(16), 3787-3807.
- Borsdorff, T., Martinez-Velarte, M. C., Sneep, M., ter Linden, M., & Landgraf, J. (2024). Random forest classifier for cloud clearing of the operational TROPOMI XCH4 product. *Remote Sensing*, 16(7), 1208.
- Butz, A., Guerlet, S., Hasekamp, O., Schepers, D., Galli, A., Aben, I., ... & Warneke, T. (2011). Toward accurate CO<sub>2</sub> and CH<sub>4</sub> observations from GOSAT. *Geophysical Research Letters*, 38(14).
- Butz, A., Hasekamp, O. P., Frankenberg, C., Vidot, J., & Aben, I. (2010). CH<sub>4</sub> retrievals from space-based solar backscatter measurements: Performance evaluation against simulated aerosol and cirrus loaded scenes. *Journal of Geophysical Research: Atmospheres*, 115(D24).
- Chen, J., Hu, R., Chen, L., Liao, Z., Che, L., & Li, T. (2024). Multi-sensor integrated mapping of global XCO<sub>2</sub> from 2015 to 2021 with a local random forest model. *ISPRS Journal of Photogrammetry and Remote Sensing*, 208, 107-120.
- Dils, B., Buchwitz, M., Reuter, M., Schneising, O., Boesch, H., Parker, R., ... & Wunch, D. (2014). The greenhouse gas climate change initiative (GHG-CCI): comparative validation of GHG-CCI SCIAMACHY/ENVISAT and TANSO-FTS/GOSAT CO<sub>2</sub> and CH<sub>4</sub> retrieval algorithm products with measurements from the TCCON. *Atmospheric Measurement Techniques*, 7(6), 1723-1744.
- East, J. D., Jacob, D. J., Balagus, N., Bloom, A. A., Bruhwiler, L., Chen, Z., ... & Zhang, Z. (2024). Interpreting the seasonality of atmospheric methane. *Geophysical Research Letters*, 51(10), e2024GL108494.
- Fan, L., Wan, Y., & Dai, Y. (2024). Development of a Multi-Source Satellite Fusion Method for XCH<sub>4</sub> Product Generation in Oil and Gas Production Areas. *Applied Sciences*, 14(23), 11100. <https://doi.org/10.3390/app142311100>
- Hasekamp, O., Lorente, A., Hu, H., Butz, A., de Brugh, J., & Landgraf, J. (2021). Algorithm theoretical baseline document for Sentinel-5 Precursor methane retrieval. *Netherlands Institute for Space Research*, 67.
- Hu, H., Landgraf, J., Detmers, R., Borsdorff, T., Aan de Brugh, J., Aben, I., ... & Hasekamp, O. (2018). Toward global mapping of methane with TROPOMI: First results and intersatellite comparison to GOSAT. *Geophysical Research Letters*, 45(8), 3682-3689
- Hwang, Y., & Song, J. (2023). Recent deep learning methods for tabular data. *Communications for Statistical Applications and Methods*, 30(2), 215-226.
- IEA (2022), World Energy Outlook 2022, IEA, Paris <https://www.iea.org/reports/world-energy-outlook-2022> , Licence: CC BY 4.0 (report); CC BY NC SA 4.0 (Annex A)



IEA (2025), Global Methane Tracker 2025, IEA, Paris <https://www.iea.org/reports/global-methane-tracker-2025>, Licence: CC  
510 BY 4.0

Inoue, M., Morino, I., Uchino, O., Nakatsuru, T., Yoshida, Y., Yokota, T., ... & Tanaka, T. (2016). Bias corrections of GOSAT SWIR XCO<sub>2</sub> and XCH<sub>4</sub> with TCCON data and their evaluation using aircraft measurement data. *Atmospheric Measurement Techniques*, 9(8), 3491-3512.

515

Imasu, R., Matsunaga, T., Nakajima, M., Yoshida, Y., Shiomi, K., Morino, I., ... & Shi, C. (2023). Greenhouse gases Observing SATellite 2 (GOSAT-2): mission overview. *Progress in Earth and Planetary Science*, 10(1), 33.

Janardanan, R., Maksyutov, S., Tsuruta, A., Wang, F., Tiwari, Y. K., Valsala, V., ... & Matsunaga, T. (2020). Country-scale analysis of methane emissions with a high-resolution inverse model using GOSAT and surface observations. *Remote Sensing*, 12(3), 375.

Jacob, D. J., Varon, D. J., Cusworth, D. H., Dennison, P. E., Frankenberg, C., Gautam, R., ... & Duren, R. M. (2022). Quantifying methane emissions from the global scale down to point sources using satellite observations of atmospheric methane. *Atmospheric Chemistry and Physics Discussions*, 2022, 1-44.

525

Kuze, A., Suto, H., Shiomi, K., Kawakami, S., Tanaka, M., Ueda, Y., ... & Buijs, H. L. (2016). Update on GOSAT TANSO-FTS performance, operations, and data products after more than 6 years in space. *Atmospheric Measurement Techniques*, 9(6), 2445-2461.

530

Kuze, A., Suto, H., Nakajima, M., & Hamazaki, T. (2009). Thermal and near infrared sensor for carbon observation Fourier-transform spectrometer on the Greenhouse Gases Observing Satellite for greenhouse gases monitoring. *Applied optics*, 48(35), 6716-6733.

Lorente, A., Borsdorff, T., Butz, A., Hasekamp, O., aan de Brugh, J., Schneider, A., ... & Landgraf, J. (2021). Methane retrieved from TROPOMI: improvement of the data product and validation of the first 2 years of measurements. *Atmospheric Measurement Techniques*, 14(1), 665-684.

Li, K., Bai, K., Jiao, P., Chen, H., He, H., Shao, L., ... & Chang, N. B. (2024). Developing unbiased estimation of atmospheric methane via machine learning and multiobjective programming based on TROPOMI and GOSAT data. *Remote Sensing of Environment*, 304, 114039.

540

Myhre, G., Shindell, D., Bréon, F. M., Collins, W., Fuglestad, J., Huang, J., ... & Zhang, H. (2014). Anthropogenic and natural radiative forcing. *Climate Change 2013-The Physical Science Basis*, 659-740.

545

Malina, E., Veihelmann, B., Buschmann, M., Deutscher, N. M., Feist, D. G., & Morino, I. (2022). On the consistency of methane retrievals using the Total Carbon Column Observing Network (TCCON) and multiple spectroscopic databases. *Atmospheric Measurement Techniques*, 15(8), 2377-2406.



- 550 Maasakkers, J. D., Jacob, D. J., Sulprizio, M. P., Scarpelli, T. R., Nesser, H., Sheng, J. X., ... & Parker, R. J. (2019). Global distribution of methane emissions, emission trends, and OH concentrations and trends inferred from an inversion of GOSAT satellite data for 2010–2015. *Atmospheric Chemistry and Physics*, *19*(11), 7859–7881.
- 555 Nisbet, E. G., Fisher, R. E., Lowry, D., France, J. L., Allen, G., Bakkaloglu, S., ... & Zazzeri, G. (2020). Methane mitigation: methods to reduce emissions, on the path to the Paris agreement. *Reviews of Geophysics*, *58*(1), e2019RG000675.
- Oshio, H., Yoshida, Y., Matsunaga, T., Deutscher, N. M., Dubey, M., Griffith, D. W., ... & Wunch, D. (2020). Bias correction of the ratio of total column ch4 to co2 retrieved from gosat spectra. *Remote Sensing*, *12*(19), 3155.
- 560 Prather, M. J., Holmes, C. D., & Hsu, J. (2012). Reactive greenhouse gas scenarios: Systematic exploration of uncertainties and the role of atmospheric chemistry. *Geophysical Research Letters*, *39*(9).
- Parker, R. J., Webb, A., Boesch, H., Somkuti, P., Barrio Guillo, R., Di Noia, A., ... & Wunch, D. (2020). A decade of GOSAT Proxy satellite CH 4 observations. *Earth System Science Data*, *12*(4), 3383–3412.
- 565 Pendergrass, D. C., Jacob, D. J., Balasus, N., Estrada, L., Varon, D. J., East, J. D., ... & Worden, J. R. (2025). Trends and seasonality of 2019–2023 global methane emissions inferred from a localized ensemble transform Kalman filter (CHEEREIO v1. 3.1) applied to TROPOMI satellite observations. *Atmospheric Chemistry and Physics*, *25*(21), 14353–14369.
- 570 Qu, Z., Jacob, D. J., Shen, L., Lu, X., Zhang, Y., Scarpelli, T. R., ... & Delgado, A. L. (2021). Global distribution of methane emissions: a comparative inverse analysis of observations from the TROPOMI and GOSAT satellite instruments. *Atmospheric Chemistry and Physics*, *21*(18), 14159–14175.
- 575 Qu, Y., Wei, J., Xing, H., Shi, X., Ao, Z., & Meng, X. (2025). Global estimates of daily gapless atmospheric XCH 4 concentrations from satellite and reanalysis data during 2003–2020. *IEEE Transactions on Geoscience and Remote Sensing*.
- Suto, H., Kataoka, F., Kikuchi, N., Knuteson, R. O., Butz, A., Haun, M., ... & Kuze, A. (2021). Thermal and near-infrared sensor for carbon observation Fourier transform spectrometer-2 (TANSO-FTS-2) on the Greenhouse gases Observing SATellite-2 (GOSAT-2) during its first year in orbit. *Atmospheric Measurement Techniques*, *14*(3), 2013–2039.
- 580 Sha, M. K., Langerock, B., Blavier, J. F. L., Blumenstock, T., Borsdorff, T., Buschmann, M., ... & Zhou, M. (2021). Validation of methane and carbon monoxide from Sentinel-5 Precursor using TCCON and NDACC-IRWG stations. *Atmospheric Measurement Techniques Discussions*, *2021*, 1–84.
- 585 Schneising, O., Buchwitz, M., Hachmeister, J., Vanselow, S., Reuter, M., Buschmann, M., ... & Burrows, J. P. (2023). Advances in retrieving XCH 4 and XCO from Sentinel-5 Precursor: improvements in the scientific TROPOMI/WFMD algorithm. *Atmospheric Measurement Techniques*, *16*(3), 669–694.
- Saunois, M., Martinez, A., Poulter, B., Zhang, Z., Raymond, P., Regnier, P., ... & Zhuang, Q. (2024). Global methane budget 2000–2020. *Earth System Science Data Discussions*, *2024*, 1–147.
- 590 Shwartz-Ziv, R., & Armon, A. (2022). Tabular data: Deep learning is not all you need. *Information Fusion*, *81*, 84–90.



- Sj, O., Cc, I., Pa, O., Lc, O., & Ai, H. (2024). Petroleum exploration in the Niger Delta region and implications for the environment: a review. *Journal of Energy Research and Reviews*, 16(5), 19-29.
- 595 Umezawa, T., Tohjima, Y., Terao, Y., Sasakawa, M., Müller, A., Saeki, T., ... & Matsueda, H. (2025). Long-term and interannual variations of atmospheric methane observed by the NIES and collaborative observation networks. *Progress in Earth and Planetary Science*, 12(1), 39.
- Veefkind, J. P., Aben, I., McMullan, K., Förster, H., De Vries, J., Otter, G., ... & Levelt, P. F. (2012). TROPOMI on the ESA  
600 Sentinel-5 Precursor: A GMES mission for global observations of the atmospheric composition for climate, air quality and ozone layer applications. *Remote sensing of environment*, 120, 70-83.
- Wunch, D., Toon, G. C., Blavier, J. F. L., Washenfelder, R. A., Notholt, J., Connor, B. J., ... & Wennberg, P. O. (2011). The  
605 total carbon column observing network. *Philosophical Transactions of the Royal Society A: Mathematical, Physical and Engineering Sciences*, 369(1943), 2087-2112.
- Worden, J. R., Cusworth, D. H., Qu, Z., Yin, Y., Zhang, Y., Bloom, A. A., ... & Jacob, D. J. (2022). The 2019 methane budget and uncertainties at 1° resolution and each country through Bayesian integration Of GOSAT total column methane data and a priori inventory estimates. *Atmospheric Chemistry and Physics*, 22(10), 6811-6841.
- 610 Wang, W., He, J., Feng, H., & Jin, Z. (2022). High-Coverage reconstruction of xco2 using multisource satellite remote sensing data in beijing–tianjin–hebei region. *International Journal of Environmental Research and Public Health*, 19(17), 10853.
- Yoshida, Y., Ota, Y., Eguchi, N., Kikuchi, N., Nobuta, K., Tran, H., ... & Yokota, T. (2011). Retrieval algorithm for CO<sub>2</sub> and CH<sub>4</sub> column abundances from short-wavelength infrared spectral observations by the Greenhouse gases observing  
615 satellite. *Atmospheric Measurement Techniques*, 4(4), 717-734.
- Yoshida, Y., Someya, Y., Ohyama, H., Morino, I., Matsunaga, T., Deutscher, N. M., ... & Wunch, D. (2023). Quality evaluation of the column-averaged dry air mole fractions of carbon dioxide and methane observed by GOSAT and GOSAT-2. *SOLA*, 19, 173-184.
- 620 Zhou, M., Dils, B., Wang, P., Detmers, R., Yoshida, Y., O'Dell, C. W., ... & De Mazière, M. (2016). Validation of TANSO-FTS/GOSAT XCO 2 and XCH 4 glint mode retrievals using TCCON data from near-ocean sites. *Atmospheric Measurement Techniques*, 9(3), 1415-1430
- 625 Zhang, Y., Gautam, R., Pandey, S., Omara, M., Maasackers, J. D., Sadavarte, P., ... & Jacob, D. J. (2020). Quantifying methane emissions from the largest oil-producing basin in the United States from space. *Science advances*, 6(17), eaaz51